ChemPubSoc Europe

DOI: 10.1002/cctc.201902045

CHEMCATCHEM Full Papers

Doping Carbon Nitride Quantum Dots into Melamine-Silver Matrix: An Efficient Photocatalyst with Tunable Morphology and Photocatalysis for H_2O_2 Evolution under Visible Light

Mengyuan Yin,[a] Xi Chen,[b] Yuqi Wan,[a] Wenwen Zhang,[a] Luping Feng,[b] Lixiang Zhang,[c] and Hua Wang*[a, b, c]

Carbon nitride quantum dots (CN_{QDs}) were doped into melamine (MA) and silver (Ag) matrix yielding CN_{QDs}@MA–Ag nanocomposites by the supramolecular self-assembly route. To our surprise, the resulting mesoporous nanocomposites could present different morphologies (i.e., nanowires, nanoflowers, and nanosheets) and especially tunable visible-light photocatalysis performances depending on the percentages of CN_{QDs} used. It was discovered that the CN_{QDs}@MA–Ag ones with the pinecone-like structure (containing 30% CN_{QDs}) could exhibit the strongest visible-light photocatalysis for splitting water to yield H_2O_2 with a production efficiency of 39.82 $\mu mol \cdot g^{-1} h^{-1}$, which is more than ten-fold higher than that of CN_{QDs} alone. Herein, the nano-scaled Ag could facilitate the increased light harvesting and the separation as well as transmission of electron-hole pairs of CN_{QDs} resulting in the enhanced visible-light photocatalysis of nanocomposites. More importantly, the pinecone-like ones might additionally enable more exposed active sites of photocatalysis and larger mesoporous specific area of contacting dissolved oxygen in water, leading to the higher photocatalytic efficiency of H_2O_2 generation. This CN_{QDs}-based fabrication strategy may open a new door towards the design of a variety of photocatalysts with different morphologies and tunable photocatalysis performances for the efficient splitting water toward H_2O_2 evolution under sunlight.

Introduction

Hydrogen peroxide (H_2O_2), an environmentally-friendly oxidant only with the final byproduct of water, has been extensively applied in the fields of environmental treatment, chemical industry, and biological process.[1–4] Traditionally, H_2O_2 is produced industrially by two kinds of routes of anthraquinone oxidation[4] and H_2 and O_2 reactions,[5] which may be trapped by some limitations like high energy consumption, tedious operation, and explosion risk. In recent years, many efforts have been alternatively devoted to the photocatalytic production of H_2O_2 due to the advantages of green sources (i.e., water and oxygen) and clean energy input (i.e., sunlight).[6–11] It is generally recognized that the performances of the photocatalytic systems may largely depend on the functional properties of photocatalysts.[12,13] As a result, how to enhance the photocatalytic functions especially the visible-light ones of photocatalysts has been being a hot topic in the current researches.[14–18] For example, Ge *et al.* utilized Ag nanoparticles to increase the visible-light photocatalytic activity of polymeric g-C_3N_4.[14] Xu and coauthors fabricated $ZnFe_2O_4$ composites in combination with Ag/AgBr showing improved photocatalysis for organic pollutant degradation.[15] Moreover, the performances of photocatalysts can largely depend on their micromorphologies and structures.[19–23] For example, Dong's group discovered that $(BiO)_2CO_3$ nanomaterials doped with different levels of thiourea could present different morphological structures and tuning photocatalysis properties.[19] Wang *et al.* have reported the fabrication of Ag_3PO_4 photocatalysts with morphologies-depending photocatalysis in the degradation of methylene blue.[20] Unfortunately, most of the current fabrication routes for the control of morphologies and structures of photocatalysts can encounter with some formidable limitations like complicated steps, limited photocatalytic activities, and harsh reaction conditions (*i.e.*, high temperature and pressure). In particular, some efforts have been devoted to the applications of surfactants with large amounts for controlling the morphological structures of photocatalysts.[24,25] A challenge regarding the limited photocatalysis of the photocatalysts might be encountered due to their surface active sites might be greatly hindered by the surfactants adsorbed. Hence, exploring a simple, efficient, and green technology for the fabrication of photocatalysts with controlled morphologies and visible-light-driven photocatalysis performances for splitting water to generate H_2O_2 evolution has been a challenging but attractive target to pursue. Besides, recent years have witnessed the rapid

[a] M. Yin, Y. Wan, W. Zhang, Prof. H. Wang
Institute of Medicine and Materials Applied Technologies
College of Chemistry and Chemical Engineering
Qufu Normal University
Qufu City 273165 (P. R. China)
Fax: +86 537 4456306
E-mail: huawang@qfnu.edu.cn
Homepage: http://wang.qfnu.edu.cn
[b] X. Chen, L. Feng, Prof. H. Wang
School of Chemistry and Chemical Engineering
Harbin Institute of Technology
Harbin 150090 (P. R. China)
[c] L. Zhang, Prof. H. Wang
School of Environment
Harbin Institute of Technology
Harbin 150090 (P. R. China)

development of various types of carbon materials like nitride quantum dots (CN_{QDs}) or g-C_3N_4 for the extensive applications of photocatalysis, adsorption, and sensing analysis due to their outstanding merits such as chemical stability, metal-free non-toxicity, cost-effectiveness, and easy preparation.[26–29] For example, Wang *et al.* have applied g-C_3N_4 for the photocatalytic hydrogen evolution from water under visible light.[27] Zhang's group have fabricated nitrogen-rich CN_{QDs} with tunable fluorescence emission by using a solid-phase reaction strategy.[26] Nevertheless, there has been no report on the use of carbon materials for tuning the morphology or structure of functional materials including photocatalysts.

Up to date, the supramolecular self-assembly route has been increasingly applications for fabrication of various functional materials.[30–34] In the previous works, we discovered that melamine (MA), an organic molecule consisting of amino groups and aromatic nitrogen atoms, could conduct the self-assembly with various heavy metal ions like Ag^+ and Cu^{2+} yielding the mesoporous nanocomposites.[33,34] In the present study, we initially doped CN_{QDs} of different levels into the MA and silver (Ag) matrix by the supramolecular self-assembly route. To our surprise, the yielded mesoporous CN_{QDs}@MA–Ag nanocomposites could present the CN_{QDs}-controlled morphologies (i.e., nanowires, nanoflowers, and nanosheets) and especially the tunable visible-light photocatalysis performances depending on the percentages of CN_{QDs} used. It was found that the nanocomposites with the pinecone-like nanoflower structure could exhibit the largest visible-light photocatalysis in splitting water towards H_2O_2 evolution. The main fabrication and photocatalytic H_2O_2 evolution procedures of CN_{QDs}@MA–Ag nanocomposites are schematically illustrated in Scheme 1 with the pinecone-like ones as example. It is thought that the nanoscaled Ag with the surface plasmon resonance (SPR) effect might increase the light harvesting as well as the separation and transmission of electron-hole pairs of CN_{QDs} leading to the enhanced visible-light photocatalysis of nanocomposites. To the best of our knowledge, this is the first report on the synthesis of the photocatalysts with CN_{QDs}-tuned morphological structures and visible-light-driven photocatalysis performances for the efficient water splitting to generate H_2O_2 under sunlight.

Results and Discussion

Fabrication and characterization of CN_{QDs}@MA-Ag with CN_{QDs}-tuned morphologies and photocatalysis performances

It is well established that MA with rich nitrogen elements (66.7%) can conduct the self-assembly with Ag^+ ions to yield the mesoporous nanocomposites.[33] In the present work, CN_{QDs} were doped with different percentages into the MA and Ag matrix to yield structure-different CN_{QDs}@MA–Ag nanocomposites by the supramolecular self-assembly route, as schematically illustrated in Scheme 1A. Figure 1 displays the SEM images of the morphological structures of the resulting CN_{QDs}@MA–Ag nanocomposites, with the amplified views of SEM images (insert). It was observed that the yielded products could present the changing morphologies, such as nanowires, nanoflowers, and nanosheets, depending on the CN_{QDs} of different percentages from 0 to 40% (Figure 1A–E).

For example, the CN_{QDs}@MA–Ag with the pinecone-like nanoflower structure could be obtained at the CN_{QDs} percentage of 30% (Figure 1D). The results indicate that CN_{QDs} with amino groups should participate the reactions between amino

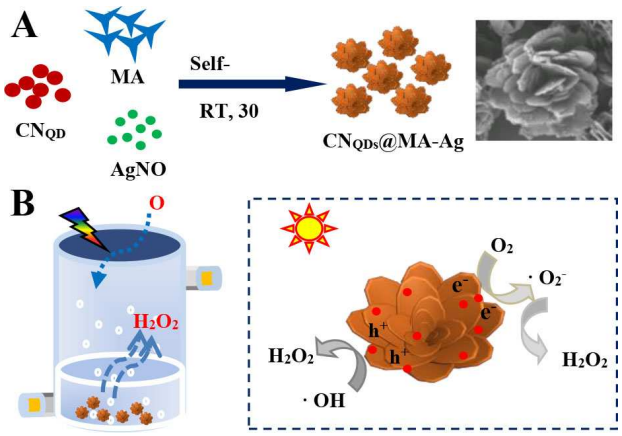

Scheme 1. Schematic illustration of (**A**) the synthesis procedure of CN_{QDs}@MA–Ag nanocomposites exemplified by pinecone-like ones with a SEM image, and (**B**) the photocatalytic H_2O_2 generation process (left) and possible mechanism (right) under sunlight.

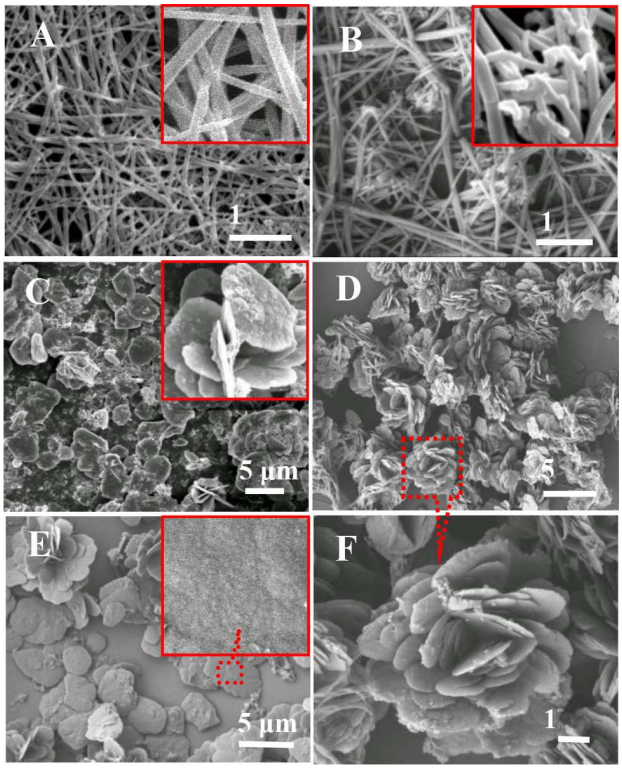

Figure 1. SEM images of and CN_{QDs}@MA–Ag nanocomposites containing different CN_{QDs} percentages of (**A**) 0% (MA–Ag), (**B**) 10%, (**C**) 20%, (**D**) 30% (with (**F**) a magnitude-amplified particle), and (**E**) 40% (insert: the magnitude-amplified views).

groups-containing MA and silver by following the supramolecular self-assembly route,[26,35] in which CN_{QDs} might competitively interact with silver to induce the MA–Ag reunion reactions with different degrees depending the percentages of CN_{QDs} used. As a result, the CN_{QDs}@MA–Ag nanocomposites would be yielded with changing morphologies typically varying from nanowires (Figure 1A) to nanosheets (Figure 1E) as increasing the CN_{QDs} percentages up to 40%. Also, the polymeric matrix of nitrogen-rich MA could allow for the controlled silver growth in nanocomposites through the strong Ag-MA chelating reactions, which might additionally aid to increase the photostability of nano-scaled Ag during the photocatalytic reactions. Moreover, Figure 2 manifests the TEM images of the pinecone-like nanocomposites by taking CN_{QDs} as the control. One can note that CN_{QDs} could be fabricated uniformly with an average size of about 4.3 nm (Figure 2A). A high crystallinity with a lattice parameter of 0.34 nm could be obtained as revealed in the amplified image (Figure 2C), which is in agreement with the 002 plane of graphitic carbon nitride previously reported.[26] Furthermore, Figure 2B manifests the TEM image of an individual nanocomposite of CN_{QDs}@MA–Ag with the pinecone-like structure, in which numerous nano-scaled Ag could be produced in the coagulated form as disclosed in the amplified view (Figure 2D).

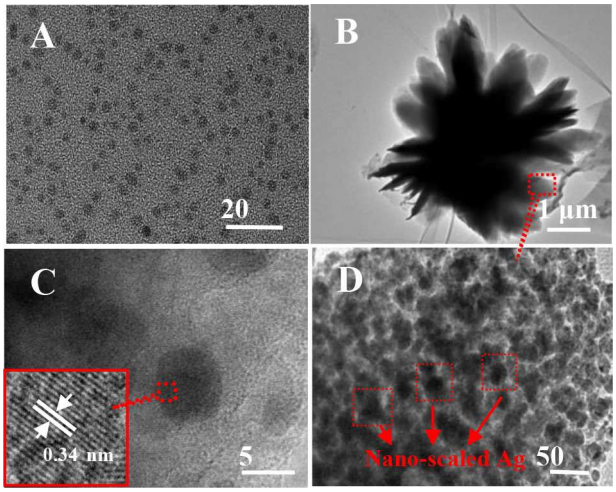

Figure 2. TEM images of (**A**) CN_{QDs} and (**B**) CN_{QDs}@MA–Ag nanocomposites with (**C**, **D**) the corresponding magnitude-amplified views indicated.

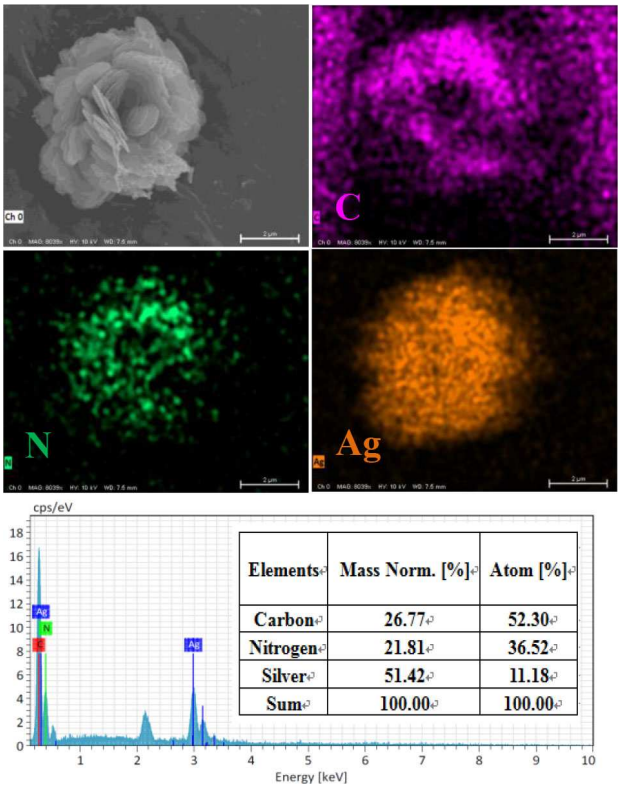

Elements	Mass Norm. [%]	Atom [%]
Carbon	26.77	52.30
Nitrogen	21.81	36.52
Silver	51.42	11.18
Sum	100.00	100.00

Figure 3. Element mapping data (C, N, and Ag) and EDS spectra of CN_{QDs}@MA–Ag nanocomposite containing 30% CN_{QDs}.

The composition of the pinecone-like nanocomposites was investigated separately by elemental mapping and EDS analysis, with the data shown in Figure 3. As expected, the C, N, and Ag elements could be distributed uniformly throughout the nanocomposites. Besides, the Brunauer-Emmett-Teller (BET) analysis was performed for the pinecone-like CN_{QDs}@MA–Ag nanocomposites in comparison with MA–Ag nanocomposites without CN_{QDs} (Figure 4). The textural surface parameters obtained from the isotherm data, i.e., BET surface area, mean pore diameter, and total pore volume, are included in Figure 4B. Accordingly, the pinecone-like CN_{QDs}@MA–Ag nanocomposites can possess apparently the mesoporous characteristics with the average pore diameter of about 5 nm. Especially, they can display the larger BET surface area than the nanocomposites without CN_{QDs}.

More importantly, the as-prepared nanocomposites with different morphological structures could exhibit the CN_{QDs}-tunable photocatalysis performances, which would be demonstrated in splitting water to generate H_2O_2 under sunlight afterwards. Figure 5A describes the UV-vis diffuse reflectance spectra (DRS) of CN_{QDs}@MA–Ag nanocomposites by taking MA–Ag nanocomposites and CN_{QDs} for comparison. To our surprise, no significant peak of UV-vis diffuse reflectance spectra could be obtained in the visible region for the CN_{QDs}@MA–Ag nanocomposites (curve c), in contrast to those for MA–Ag (curve a) and CN_{QDs} (curve b) exhibiting the large peaks in the

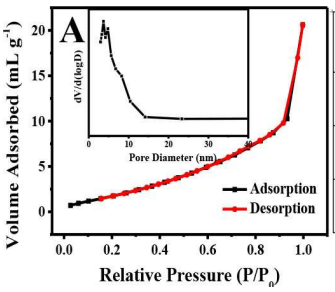

B Samples	CN_{QDs}@MA-Ag	MA-Ag
BET surface area ($m^2 g^{-1}$)	17.792	15.587
Mean pore diameter (nm)	5.08	3.76
Total pore volume (mL g^{-1})	0.0319	0.0168

Figure 4. (**A**) The N_2 sorption isotherms of BET analysis for the pinecone-like CN_{QDs}@MA–Ag nanocomposites containing 30% CN_{QDs} (insert: the corresponding pore size distribution curve). (**B**) Textural surface parameters from N_2 adsorption-desorption isotherms measured from the photocatalysts.

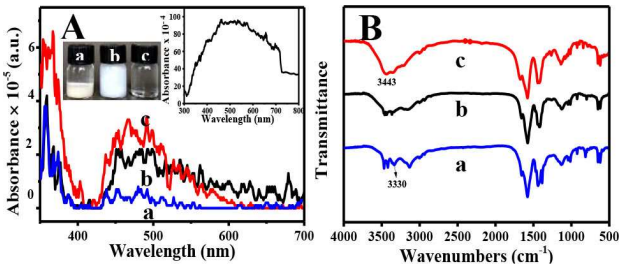

Figure 5. Comparison of (**A**) UV-vis spectra and (**B**) FTIR among (a) CN_{QDs}@MA–Ag nanocomposites, (b) MA–Ag, and (c) CN_{QDs} (insert: the corresponding photographs and the one used after photocatalytic H_2O_2 generation reaction).

visible region. Moreover, as visually illustrated in the photographs (Figure 5A, insert), the MA–Ag nanocomposites could be produced as the white suspensions. When CN_{QDs} were introduced into the MA–Ag reaction matrix, the resulted CN_{QDs}@MA–Ag nanocomposites could be formed as the light yellow precipitates, with the changed morphologies revealed in the SEM images above (Figure 1). Accordingly, the CN_{QDs}@MA–Ag nanocomposites could be yielded substantially as new nanocomposites during the CN_{QDs}-tuned self-assembly of MA and silver matrix, which might otherwise be formed as the nanowires-shaped products in the absence of CN_{QDs} as aforementioned (Figure 1A). Besides, it should be pointed out that when the CN_{QDs}@MA–Ag nanocomposites were applied for the photocatalytic splitting of water for H_2O_2 evolution under sunlight, the enhanced absorption could be observed for the used nanocomposites showing the broadened UV-vis diffuse emission in the visible region (Figure 5A, insert), due to that nano-scaled Ag might be increasingly formed during the illumination procedure. Importantly, such a broadening of the visible-light response region of nanocomposites would help to further improve their light harvesting or the utilization efficiency of solar energy, as confirmed elsewhere for other kinds of photocatalysts.[36–38]

In addition, a comparison of the FTIR spectra was conducted among the CN_{QDs}@MA–Ag nanocomposites, CN_{QDs}, and MA–Ag nanocomposites (Figure 5B). It is found that all of the samples could possess the peaks ranging from 1200 to 1650 cm^{-1} that may belong to the typical stretching modes of C–N heterocycles. The broad peak around 3300 cm^{-1} (curve a) can be assigned to the stretching vibration of -NH or $-NH_2$ groups of MA there. Moreover, as shown in Figure 5B, the amounts of $-NH_2$ groups could be increased in the CN_{QDs}@MA–Ag nanocomposites (curve c), which might aid to further improve the hydrophilicity of the nanocomposites to facilitate the promoted electron transferring of nanocomposites, as described for N-doped carbon nanofibers elsewhere,[39] which might lead to the increased photocatalysis of CN_{QDs}@MA–Ag nanocomposites for H_2O_2 evolution afterwards.

Investigations on the photogenerated carriers behaviors of CN_{QDs}@MA-Ag nanocomposites containing different CN_{QDs} percentages

The photogenerated carriers behaviors of CN_{QDs}@MA–Ag nanocomposites containing different CN_{QDs} percentages (morphological structures) were explored comparably by monitoring the separation rates and transferring performances of photogenerated electron-hole pairs by using electrochemical impedance spectroscopy (EIS) and transient photocurrent experiments (Figure 6). As can be seen from Figure 6A, the lowest resistance of charge transferring, which can be reflected by the frequency semicircles in the EIS Nyquist diagram, could be obtained for the pinecone-like nanocomposites containing 30% CN_{QDs}, showing the superior charge transfer capability. Furthermore, Figure 6B reveals the transient photocurrent response curves of the morphology-different nanocomposites on the typical cycles of visible light irradiation on or off, in which the 0% refers to MA–Ag nanocomposites for the blank control. One can note that with the light on, all of the CN_{QDs}@MA–Ag nanocomposites could immediately produce the photocurrents under visible light irradiation, in contrast to the MA–Ag nanocomposites with no significant change in photocurrent. The data demonstrate that CN_{QDs} could endow the CN_{QDs}@MA–Ag nanocomposites with the enhanced photo-sensitivity and more efficient spatial charge separation. In particular, the pinecone-like CN_{QDs}@MA–Ag (containing 30% CN_{QDs}) could display the largest transient photocurrents, promising the strongest capacity of photocatalytic splitting water to yield H_2O_2 under sunlight.

Photocatalytic H_2O_2 generation performances of CN_{QDs}@MA-Ag nanocomposites containing different CN_{QDs} percentages

The photocatalytic performances of CN_{QDs}@MA–Ag nanocomposites containing different CN_{QDs} percentages (morphological structures) were comparably evaluated by the H_2O_2 concentrations produced in the photocatalytic water splitting (Figure 7), in which a standard curve for H_2O_2 determination was scheduled (Figure 7A). Figure 7B shows the variation of H_2O_2 concentrations for the tested CN_{QDs}@MA–Ag photocatalysts containing different CN_{QDs} percentages, taking CN_{QDs} and

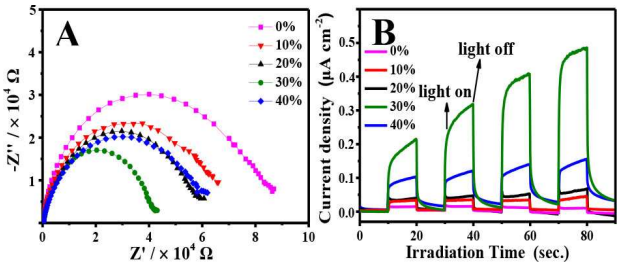

Figure 6. Comparison of (**A**) EIS plots and (**B**) transient photocurrent curves among the CN_{QDs}@MA–Ag nanocomposites with the CN_{QDs} percentages of 0%, 10%, 20%, 30%, and 40%.

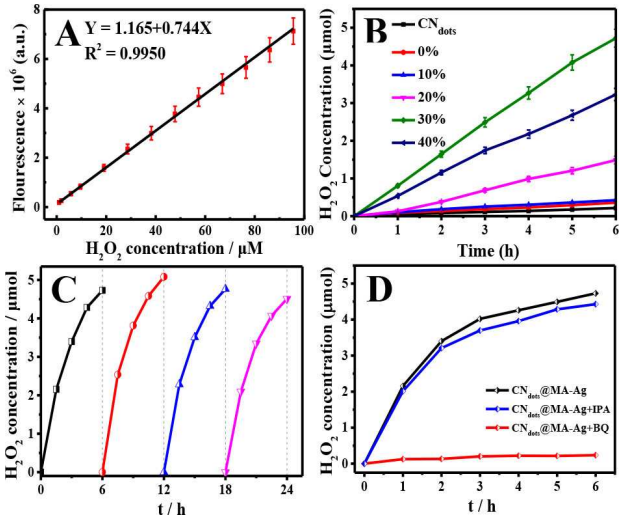

Figure 7. (**A**) The calibration curve of fluorescence intensities versus different H_2O_2 concentrations. (**B**) The illumination time-depending H_2O_2 concentrations yielded in the photocatalyzed reactions with the CN_{QDs}@MA–Ag containing different CN_{QDs} percentages. (**C**) The results of photostability for the pinecone-like CN_{QDs}@MA–Ag during the four-run photocatalytic reactions for H_2O_2 production. (**D**) The results of reactive species-trapping experiments for the pinecone-like CN_{QDs}@MA–Ag separately in the absence and presence of 1.0 mM BQ and 1.0 mM IPA.

MA–Ag nanocomposites (0% CN_{QDs}) for comparison. One can see from Figure 7B that the CN_{QDs}@MA–Ag nanocomposites could present changing H_2O_2 levels in the photocatalytic water splitting reactions, which are much higher than those of the ones photocatalyzed by MA–Ag nanocomposites or pure CN_{QDs}. More interestingly, the strongest photocatalysis was achieved for the pinecone-like nanocomposites containing 30% CN_{QDs} with a H_2O_2 production efficiency of 39.82 $\mu mol \cdot g^{-1} h^{-1}$ so calculated, over which the higher CN_{QDs} percentages in the nanocomposites would trigger a decrease in the H_2O_2 concentrations produced. In addition, it is noteworthy from Figure 7B that the efficiency of pure CN_{QDs} in the photocatalytic H_2O_2 production was obtained to be 2.256 $\mu mol \cdot g^{-1} h^{-1}$, which is much lower than that of CN_{QDs}@MA–Ag nanocomposites. Herein, it is thought that too higher CN_{QDs} percentages (i.e., over 40%) might bring too $-NH_2$ amounts into the nanocomposites so as to form a recombination center for the photogenerated electron-hole pairs, resulting in a decrease in the photocatalysis active sites of nanocomposites. Also, as aforementioned above, the pinecone-like three-dimensional (3D) structure of CN_{QDs}@MA–Ag with 30% CN_{QDs} might enable the most exposed active sites of photocatalysis and the largest specific area for contacting dissolved oxygen in water, thus leading to the enhanced photocatalysis for H_2O_2 generation.

Although the detailed mechanism should be further explored, the introduction of CN_{QDs} with the suitable levels in nanocomposites should be beneficial for achieving the morphology-dependent adsorption capacity and especially the efficient photocatalysis in the splitting of water towards H_2O_2 generation under sunlight.

The photostability of the CN_{QDs}@MA–Ag nanocomposites was studied by using the pinecone-like ones as example, in which four consecutive runs of photocatalytic water splitting reactions were conducted under visible light irradiation (Figure 7C). It was observed that the H_2O_2 production could show no significant change during the four runs of illumination experiments. Such a high photostability of the photocatalysts may promise for long-term applications due to the polymeric matrix of MA for nano-scaled Ag and CN_{QDs} in nanocomposites as aforementioned. Moreover, the trapping experiments were performed for active species yielded in the photocatalytic water splitting reactions separately by using p-benzoquinone (BQ) and isopropanol (IPA) as the capture agents for $^{\bullet}O^{2-}$ and $^{\bullet}OH$ free radicals, respectively (Figure 7D). It was witnessed that the photocatalytic reactions could be completely restrained by BQ showing the dramatically decreased H_2O_2 amounts. The results indicate that the generation of H_2O_2 could be resulted from the formation of $^{\bullet}O^{2-}$ free radicals during the photocatalytic water splitting reactions. To further confirm such a fact, the $^{\bullet}OH$ removal experiments were carried out by using the $^{\bullet}OH$ quencher of IPA. As expected, no obvious decrease in the H_2O_2 production was observed. Therefore, the photocatalysis process of CN_{QDs}@MA–Ag nanocomposites in splitting water to produce H_2O_2 might be mainly dominated by the reduction of photogenerated electrons rather than the oxidation of holes of the photocatalysts.

CN_{QDs}-tuned formation process and photocatalytic H_2O_2 generation mechanism of CN_{QDs}@MA-Ag nanocomposites

Based on the results above, the CN_{QDs}-tuned self-assembly process and photocatalytic H_2O_2 generation mechanism of CN_{QDs}@MA–Ag nanocomposites are schematically illustrated in Scheme 1 using the pinecone-like ones as the model. As shown in Scheme 1A, CN_{QDs} synthesized under the NH_3 atmosphere should possess rich nitrogen atoms that can interact with silver elements, so does the nitrogen-rich polymer molecule of MA. Once CN_{QDs} were introduced into the MA and Ag matrix, a supramolecular self-assembly process would be triggered to yield the nanocomposites showing the different morphological structures regulated by CN_{QDs}. Moreover, a photocatalytic H_2O_2 generation mechanism is thereby proposed for the developed photocatalysts of CN_{QDs}@MA–Ag nanocomposites as illustrated in Scheme 1B. Under the visible light irradiation, the CN_{QDs}@MA–Ag nanocomposites should be excited to generate the electrons and holes with efficient spatial separation. As revealed by reactive species-trapping experiments above, herein, the superoxide ($^{\bullet}O_2^-$) so yielded should play a major role in photocatalytic splitting water to generate H_2O_2. Accordingly, the dissolved oxygen in water should mainly react with the excited electrons to restore O_2 into $^{\bullet}O_2^-$, which should be further reduced into H_2O_2, with the photocatalytic reactions described as follows:

$$O_2 + e^- \rightarrow {}^{\bullet}O_2^- + e^- \rightarrow H_2O_2 \quad (1)$$

$$^{\bullet}OH + h^{+} \rightarrow H_2O_2 \quad (2)$$

Besides, it is thought that new photocatalysis active sites of the synergistic CN_{QDs} and nano-scaled Ag might be produced in the CN_{QDs}@MA–Ag nanocomposites. In particular, during the photocatalytic H_2O_2 generation, the nanocomposites with the pinecone-like structure may enable more exposed photocatalytic active sites and larger specific area for contacting with the dissolved oxygen in water, thus achieving the higher efficiency of H_2O_2 generation under visible light irradiation.

Conclusions

In summary, CN_{QDs} were successfully doped into the MA–Ag matrix yielding the mesoporous CN_{QDs}@MA–Ag nanocomposites for the efficient photocatalytic H_2O_2 evolution under sunlight. It was discovered that the resulting nanocomposites could present the different morphologies changing from one-dimensional nanowires to three-dimensional nanoflowers or nanosheets depending on the percentages of CN_{QDs} used. More interestingly, CN_{QDs}-tuned photocatalysis activities could be expected for the CN_{QDs}@MA–Ag nanocomposites in splitting water to produce H_2O_2 under visible light. It is thought that the nano-scaled Ag with the SPR effect might increase the light harvesting as well as the separation and transmission of electron-hole pairs of CN_{QDs} by forming new photocatalysis active sites in nanocomposites with enhanced photocatalysis. In particular, the pinecone-like CN_{QDs}@MA–Ag (containing 30% CN_{QDs}) could exhibit the highest photocatalytic efficiency of H_2O_2 generation, which is more than ten-fold higher than that of pure CN_{QDs} alone, due to that the 3D structure of nanoflowers might enable more exposed active sites of photocatalysis and larger mesoporous specific area of contacting dissolved oxygen in water. Yet, the detailed mechanism for the morphology-depending photocatalysis should be further explored. Besides, it was demonstrated that the developed CN_{QDs}@MA–Ag photocatalysts could display the high photostability because of the polymeric matrix of MA that might conduct the strong interactions with nano-scale Ag in nanocomposites. Therefore, the developed mesoporous photocatalytic nanocomposites may promise for the extensive applications in the fields of industry photocatalysis, adsorption separation, and environmental water treatments (i.e., pollutant degradation). Importantly, such a CN_{QDs}-based fabrication strategy may provide a general route for the design of various photocatalysts and/or solid sorbents with tunable adsorption morphologies and visible-light-driven photocatalysis performances.

Experimental Section

Reagents and apparatus

Melamine (MA), silver nitrate ($AgNO_3$), sodium citrate, urea, nitric acid, potassium hydrogen phthalate and isopropanol (IPA, 99.7%) were purchased from Sinopharm Chemical Reagent Co. (China). Horseradish peroxidase (HRP) was bought from Sangon Biotech Co., Ltd. (Shanghai, China). The p-hydroxyphenylacetic acid (HPAA) and p-benzoquinone (BQ, 97%) were purchased from Sigma-Aldrich Co. Ltd. (Shanghai, China). All other reagents are of analytical grade. Deionized water (>18 Mohm) was obtained from an Ultrapure water system (Pall, USA). All glass containers were cleaned in turn by aqua regia and ultrapure water.

The morphological and elemental mapping measurements were conducted for the functional materials or products using a scanning electron microscope (SEM, Hitachi E-1010, Horiba Ex-250) with a microanalysis system (EDAX, USA), high-resolution transmission electron microscopy (HRTEM, Tecnai G20, FEI, USA), UV-vis diffuse reflectance spectra (DRS, Shimadzu/UV-3600, Japan), and Fourier transform infrared (FTIR) spectrophotometer (Thermo Nicolet Nexus 470FT, USA). The amounts of hydrogen peroxide (H_2O_2) produced in pure water were monitored by measuring the fluorescent products of catalytic H_2O_2-HPAA reactions using the fluorescence spectrometer (Horiba, FluoroMax-4, Japan). Electrochemical impedance spectroscopy (EIS) and transient photocurrent experiments were performed with an electrochemical workstation CHI 760D (CH Instrument, Shanghai, China) connected to a personal computer. A three-electrode system was applied consisting of a glassy carbon working electrode, which was first polished with alumina powder and then ultrasonically cleaned with water and alcohol, a Pt wire counter electrode, and an Ag/AgCl reference electrode.

Brunauer-Emmett-Teller (BET) surface area was measured by nitrogen adsorption-desorption method using a specific surface area and pore size analyzing instrument (Kubo-x1000).

Synthesis of photocatalyst materials

Synthesis of CN_{QDs}

Carbon nitride quantum dots (CN_{QDs}) were synthesized according to a modified procedure previously reported.[26] Briefly, 0.101 g urea and 0.081 g sodium citrate were thoroughly ground into the powders in an agate mortar in dry environment to be uniformly mixed. Then, the mixed powders were transferred into a Teflon-lined autoclave to be heated at 180 °C for 1 h. After that, the reaction vessel was stewed overnight in the atmosphere NH_3 discharged from urea. Furthermore, the obtained yellowish products were washed for three times with ethanol, and finally dried in an oven at 60 °C for further usage.

Synthesis of CN_{QDs}@MA-Ag nanocomposites

The CN_{QDs}@MA–Ag nanocomposites were synthesized by the controlled supramolecular self-assembly procedure using CN_{QDs} of different percentages. Briefly, under vigorous stirring, an aliquot of MA (50.4 mg) was dissolved in 10 mL water at 60 °C, followed by addition of CN_{QDs} of different amounts (9.37, 21.08, 36.13, and 56.2 mg). After being cooled down to room temperature, 10 mL $AgNO_3$ (20 mM) was separately introduced into each of the mixtures to be aged for 1 h. Afterwards, the mixtures were centrifuged for about 15 min at 4000 rpm, and then washed with water and alcohol, each for three times. Subsequently, the light yellow products of CN_{QDs}@MA–Ag nanocomposites were collected to be dried under vacuum and then stored in dark for further usage. In addition, the BET surface areas of CN_{QDs}@MA–Ag nanocomposites were measured by the nitrogen adsorption-desorption method.

Photocatalytic H_2O_2 generation experiments

The photocatalytic activities of the functional materials were evaluated under the visible light irradiation, in which a 300 W Xenon lamp with a 420 nm cutoff filter was applied as the visible light source. During each of the photocatalytic experiments, an aliquot of 0.020 g photocatalyst samples was initially dispersed into 10 mL water in a container with cooling water jacket outside. Prior to the visible light irradiation, the photocatalytic reaction proceeded in dark by stirring for 1 h to ensure the adsorption-desorption equilibrium among the photocatalysts, dissolved oxygen, and water. Moreover, the continuous irradiation was carried out to trigger the photocatalytic reactions for H_2O_2 evolution. An aliquot of 0.50 mL suspensions was taken from the reaction system at the given time intervals of one hour. After the centrifugation for removing the photocatalyst precipitations, the fluorescent measurements of the products of catalytic H_2O_2-HPAA reactions were performed according to a fluorometric analysis method previously reported.[7]

Acknowledgements

This work is supported by the National Natural Science Foundations of China (No. 21675099); Major Basic Research Program of Natural Science Foundation of Shandong Province (ZR2018ZC0129), and Key R&D Plan of Jining City (2018HMNS001), Shandong, P. R. China.

Keywords: Carbon nitride quantum dots · Morphology control · Photocatalysis · Silver-melamine matrix · Water splitting

[1] J. Xu, Z.-Y. Chen, H.-W. Zhang, G.-B. Lin, H.-X. Lin, X.-X. Wang, J.-L. Long, *Sci. Bull.* **2017**, *62*, 610–618.
[2] S. Kim, G. Moon, H. Kim, Y. Mun, P. Zhang, J. Lee, W. Choi, *J. Catal.* **2018**, *357*, 51–58.
[3] Y. Shiraishi, Y. Kofuji, H. Sakamoto, S. Tanaka, S. Ichikawa, T. Hirai, *ACS Catal.* **2015**, *5*, 3058–3066.
[4] J.-M. Campos-Martin, G. Blanco-Brieva, J.-. L.-G. Fierro, *Angew. Chem. Int. Ed.* **2006**, *45*, 6962–6984; *Angew. Chem.* **2006**, *118*, 7116–7139.
[5] S.-J. Freakley, Q. He, J.-. H. Harrhy, L. Lu, D.-. A. Crole, D.-. J. Morgan, E.-. N. Ntainjua, J.-. K. Edwards, A.-. F. Carley, A.-. Y. Borisevich, C.-. J. Kiely, G.-. J. Hutchings, *Science.* **2016**, *351*, 965–968.
[6] L.-H. Zheng, H.-R. Su, J. Z. Zhang, L.-S. Walekara, H.-V. Molamahmood, B. X. Zhou, M.-C. Long, Y.-H. Hua, *Appl. Catal. B* **2018**, *239*, 475–484.
[7] S.-N. Li, G.-H. Dong, R. Haililia, L.-P. Yang, Y.-X. Li, F. Wang, Y.-B. Zeng, C.-Y. Wang, *Appl. Catal. B* **2016**, *190*, 26–35.
[8] L.-P. Yang, G.-H. Dong, D.-L. Jacobs, Y.-H. Wang, L. Zang, C.-Y. Wang, *J. Catal.* **2017**, *352*, 274–281.
[9] W.-C. Hou, Y.-S. Wang, *ACS Sustainable Chem. Eng.* **2017**, *5*, 2994–3001.
[10] Y. Yang, C. Zhang, D.-L. Huang, G.-M. Zeng, J.-H. Huang, C. Lai, C.-Y. Zhou, W.-J. Wang, H. Guo, W.-J. Xue, R. Deng, M. Cheng, W.-P. Xiong, *Appl. Catal. B* **2019**, *245*, 87–99.
[11] L. Shi, L.-Q. Yang, W. Zhou, Y.-Y. Liu, L.-S. Yin, X. Hai, H. Song, J.-H. Ye, *Small* **2018**, *14*, 1703142–1703150.
[12] K. Zhu, M.-Q. Zhang, X.-Y. Feng, L.-X. Qin, S.-Z. Kang, X. Q. Li, *Appl. Catal. B* **2019**, 118434.
[13] H.-G. Kim, D.-W. Hwang, J.-S. Lee, *J. Am. Chem. Soc.* **2004**, *126*, 8912–8913.
[14] L. Ge, C.-C. Han, J. Liu, Y.-F. Li, *Appl. Catal. A* **2011**, *409*, 215–222.
[15] Y.-G. Xu, Q.-Q. Liu, C.-C. Liu, Y.-P. Zhai, M. Xie, L.-Y. Huang, H. Xu, H.-M. Li, J.-J. Jing, *J. Colloid Interface Sci.* **2018**, *512*, 555–566.
[16] F.-Y. Xu, K. Meng, B. Cheng, J.-G. Yu, W.-K. Ho, *ChemCatChem* **2019**, *11*, 465–472.
[17] Z.-T. Ge, A.-C. Yu, R. Lu, *Mater. Lett.* **2019**, *250*, 9–11.
[18] S.-S. Dong, C. Liu, Y.-G. Chen, *J. Colloid Interface Sci.* **2019**, *553*, 59–70.
[19] F. Dong, Q.-Y. Li, Y.-J. Sun, W.-K. Ho, *ACS Catal.* **2014**, *4*, 4341–4350.
[20] B. Wang, L. Wang, Z.-B. Hao, Y. Luo, *Catal. Commun.* **2015**, *58*, 117–121.
[21] J. Singh, K. Sahu, S. Mohapatra, *J. Phys. Chem. Solids* **2019**, *129*, 317–323.
[22] R. Hailili, X.-X. Yuan, C.-Y. Wang, *Catal. Today* **2019**, *335*, 591–598.
[23] B. Babu, B. Akkinepally, J. Shim, K. Yoo, *Ceram. Int.* **2019**, *45*, 15178–15187.
[24] S. Rahut, S.-S. Basu, J.-K. Basu, *CrystEngComm* **2019**, *21*, 23–29.
[25] Z.-H. Liu, Y.-J. Zheng, T.-T. Gao, J. Zhang, X. F. Sun, G.-W. Zhou, *Int. J. Hydrogen Energy* **2017**, *42*, 21775–21785.
[26] J. Zhou, Y. Yang, C.-Y. Zhang, *Chem. Commun.* **2013**, *49*, 8605–8607.
[27] X. Wang, K. Maeda, X. Chen, K. Takanabe, K. Domen, Y. Hou, X. Fu, M. Antonietti, *J. Am. Chem. Soc.* **2009**, *131*, 1680–1681.
[28] H. Liu, D. Yu, T. Sun, H. Du, W. Jiang, Y. Muhammad, L. Huang, *Appl. Surf. Sci.* **2019**, *473*, 855–863.
[29] P. Kumar, E. Vahidzadeh, U. Thakur, P. Kar, K. Alam, A. Goswami, N. Mahdi, K. Cui, G. Bernard, V. Michaelis, *J. Am. Chem. Soc.* **2019**, *141*, 5415–5436.
[30] S. Shang, B.-H. Yuan, Y.-R. Sun, G.-Q. Chen, C.-Y. Huang, B. Yu, S. He, H.-M. Dai, X.-F. Chen, *J. Colloid Interface Sci.* **2019**, *553*, 364–371.
[31] Y. Xiao, J.-X. Zhang, M.-D. Lang, *Polym. Sci., Part A: Polym. Chem.* **2018**, *56*, 789–796.
[32] R.-S. Bhosale, D.-D. La, S.-D. Padghan, M.-A. Kobaisi, L.-A. Jones, S.-V. Bhosale, S.-V. Bhosale, *ChemistrySelect* **2017**, *2*, 10118–10122.
[33] M. Liu, L.-Y. Zhang, Y. Hua, L.-P. Feng, Y. Jiang, X.-J. Ding, W. Qi, H. Wang, *Anal. Chem.* **2017**, *89*, 9552–9558.
[34] Y. Hua, M. Liu, S. Li, F.-L. Liu, Y.-Y. Cai, H. Liu, Y.-Q. Wan, X.-X. Lv, H. Wang, *Biosens. Bioelectron.* **2019**, *124*, 89–95.
[35] J. Fei, L. Gao, J. Zhao, C.-L. Du, J.-B. Li, *Small* **2013**, *9*, 1021–1024.
[36] Y. Chen, W. Huang, D. He, Y. Situ, H. Huang, *ACS Appl. Mater. Interfaces* **2014**, *6*,14405–14414.
[37] D. Ojhaa, H. Karkia, J. Songa, H. Kim, *Compos. Part B* **2019**, *160*, 277–284.
[38] M. Cheng, S. Yang, R. Chen, X. Zhu, Q. Liao, Y. Huang, *Mol. Cancer* **2018**, *448*, 185–194.
[39] Z. He, M.-M. Li, Y.-H. Li, L. Wang, J. Zhu, W. Meng, C.-C. Li, H.-Z. Zhou, L. Dai, *Appl. Surf. Sci.* **2019**, *469*, 423–430.

Manuscript received: October 29, 2019
Revised manuscript received: December 3, 2019
Version of record online: January 8, 2020